





Link between packing morphology and the distribution of contact forces and stresses in packings of highly nonconvex particles

N. A. Conzelmann ^{1,2} A. Penn,¹ M. N. Partl ² F. J. Clemens,² L. D. Poulikakos ² and C. R. Müller ¹

¹*ETH Zürich, Laboratory of Energy Science and Engineering, Department of Mechanical and Process Engineering, Institute of Energy and Process Engineering, Leonhardstrasse 21, 8092 Zürich, Switzerland*

²*Empa—Swiss Federal Laboratories for Materials Science and Technology, Überlandstrasse 129, 8600 Dübendorf, Switzerland*



(Received 17 August 2020; revised 23 November 2020; accepted 24 November 2020; published 21 December 2020)

An external load on a particle packing is distributed internally through a heterogeneous network of particle contacts. This contact force distribution determines the stability of the particle packing and the resulting structure. Here, we investigate the homogeneity of the contact force distribution in packings of highly nonconvex particles both in two-dimensional (2D) and three-dimensional (3D) packings. A recently developed discrete element method is used to model packings of nonconvex particles of varying sphericity. Our results establish that in 3D packings the distribution of the contact forces in the normal direction becomes increasingly heterogeneous with decreasing particle sphericity. However, in 2D packings the contact force distribution is independent of particle sphericity, indicating that results obtained in 2D packings cannot be extrapolated readily to 3D packings. Radial distribution functions show that the crystallinity in 3D packings decreases with decreasing particle sphericity. We link the decreasing homogeneity of the contact force distributions to the decreasing crystallinity of 3D packings. These findings are complementary to the previously observed link between the heterogeneity of the contact force distribution and a decreasing packing crystallinity due to an increasing polydispersity of spherical particles.

DOI: [10.1103/PhysRevE.102.062902](https://doi.org/10.1103/PhysRevE.102.062902)

I. INTRODUCTION

Densely packed granular materials are frequently encountered in everyday life, for example, in civil engineering applications such as railway track ballast or porous asphalt pavements [1,2]. Such packings often undergo compaction either by forced compression or due to the material's own weight [3,4]. It has been well established that internal forces in packed granular materials are not distributed homogeneously [5,6] but, instead, forces are transmitted within the material through a network of so-called force chains. This force chain network traverses through the whole particle packing, but transmits forces through only a subset of the packed particles that are subject to above-average loads [7,8]. When exceeding a critical stress value in a force chain, buckling and/or slipping events can occur which result in large scale rearrangements of the packing [9,10]. Hence, the topology of the force chain network critically affects the structural stability of the packing [11].

Studies on force chains can be largely categorized into studies that consider (i) two-dimensional (2D) packings [6,7], i.e., packings comprising only one particle layer, or three-dimensional (3D) packings [5,12]; and (ii) packings that are compressed or sheared [6,7,12]. Compressed packings are obtained either by the uniaxial compression of particles in a rigid-walled container via a moving piston [12,13], or by its isotropic compression via two perpendicular walls [6,14]. To shear stress packings, various methods are used, for example, placing particles in a rectangular confinement and compressing in one direction while expanding in another direction

[6]. Numerically, packings may be sheared by compressing the packing vertically, while introducing a constant horizontal velocity to a frictional top wall and allowing a free horizontal movement of the particles [14,15].

In 2D packings, force chains were first qualitatively and later quantitatively probed by transmitting polarized light through a sheared packing of photoelastic disks, visualizing the stress in the disks in the form of fringes [7,16]. This method was extended by Liu *et al.* [5] to 3D packings by immersing photoelastic beads in a liquid with a matching refractive index. It was found that the magnitude of the contact forces is distributed heterogeneously through the packing. To this date, there is no agreement on how to quantify force chains, but commonly the distribution of contact forces is quantified by the probability distributions of the contact forces [5,12,17]. For example, Liu *et al.* [5] placed carbon paper onto the inner surfaces of a container holding a particle packing. By calibrating the size of the imprints on the carbon paper against a known force they obtained the probability distribution $P(f)$ with $f = F_n / \langle F_n \rangle$ of the normal contact forces (F_n) normalized by the mean normal contact force ($\langle F_n \rangle$). It was found that the probability of finding large normalized forces (i.e., $f > 1$) decays exponentially with increasing force magnitude. To explain this experimental observation, a theoretical model was proposed that assumes that the dominant mechanism which gives rise to force chains is governed by the heterogeneity of the granular packing, causing in turn, an unequal force distribution on the individual particles. It was observed further that $P(f)$ has a peak at $f = 1$ and that $P(f) \rightarrow 0$ for $f \rightarrow 0$. The shape of the observed probability distribution function of the

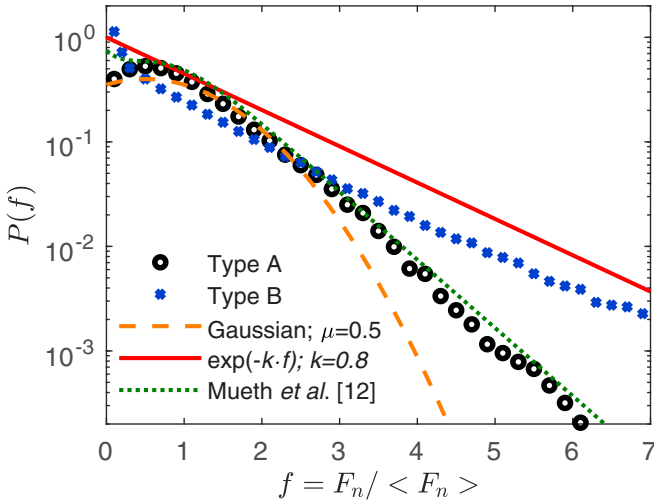


FIG. 1. Probability distributions of f , i.e., the normal contact force (F_n) normalized by the mean normal contact force ($\langle F_n \rangle$). Distributions of type A and B represent characteristic shapes that have been observed in various particle packings. The type A and type B distributions were obtained for 3D packings studied in this work. Specifically, a type A distribution was obtained for spheres and a type B distribution for star-shaped particles with a sphericity (Ψ) equal to 0.419.

contact forces resembles a characteristic shape commonly observed for disk- and sphere-shaped particles [5,12,13,15,17]. This characteristic shape is shown schematically in Fig. 1 and labeled as type A, while the characteristic distribution labeled type B is, for example, observed in sheared packings of nonspherical particles [14,15]. A shortcoming of the carbon paper method is the difficulty of distinguishing between beads that do not transmit a force and voids. This aspect was studied further by Mueth *et al.* [12], determining the fraction of contacts in compressed 3D packings that transmit forces that are sufficiently low to not leave an imprint on the carbon paper. Incorporating this additional information, Mueth *et al.* [12] found that $P(f)$ has a saddle point at $f = 1$ and $P(f)$ increases for $f \rightarrow 0$ instead of approaching zero as proposed by Liu *et al.* [5]. Hence, for $f > 0.5$ the $P(f)$ as observed by Mueth *et al.* [12] has a concave shape that is characteristic of a distribution of type A, but combined with an increasing probability for $f \rightarrow 0$, that is characteristic for a type B distribution (Fig. 1). The previous observation of Liu *et al.* [5] that $P(f)$ decays exponentially for $f > 1$ was confirmed by Mueth *et al.* [12].

Currently, there is no agreement on the mathematical function that best describes $P(f)$. While some authors have argued that in a packing of spheres (type A shown in Fig. 1) $P(f)$ can be fitted best by a Gaussian distribution [13,18], Mueth *et al.* [12] proposed Eq. (1) since a saddle point rather than a peak (at $f \approx 1$) was observed.

$$P(f) = a(1 - be^{-f^2})e^{-\beta f}. \quad (1)$$

In this equation a , b , and β are fitting parameters. However, as shown in Fig. 1, neither a Gaussian function nor Eq. (1) describes force distributions that have a type B shape. Nonetheless, it is generally agreed that for $f > 1$, $P(f)$ decays

exponentially, independent of the domain dimensionality and particle sphericity. This observation motivated Azéma and Radjai [15] to propose the following fit to the tail ($f > 1$) of $P(f)$:

$$P(f) = e^{-kf}, \quad f > 1. \quad (2)$$

Here, the exponent k is a fitting parameter that will be used to quantify the length of the exponential tail of $P(f)$.

Majmudar and Behringer [6] further improved the quantification of the magnitude of contact forces by using photoelastic disks and acquiring high-resolution photographs of 2D packings, allowing them to distinguish the individual interference fringes in the disks. Solving an inverse problem, which relates the number of fringes observed in a disk to the magnitude of the contact forces, the normal and tangential contact forces at each contact point were determined. Using this improved experimental technique, it was observed that in sheared packings fewer particles transmit large forces compared to compressed packings leading to more distinct force chains. Furthermore, it was shown that $P(f)$ in sheared and compressed packings of disks resembles a type A distribution with a peak at $f \approx 1$. However, the coefficient k of the exponential decay is smaller for sheared packings when compared to compressed packings.

Despite the continuous development and improvement of experimental techniques to visualize and quantify contact forces, it remains challenging to extract quantitative information of contact forces, in particular in 3D packings that are of high practical relevance. To address these challenges, the discrete element method (DEM) has established itself as an alternative to experimental approaches [19], providing detailed information on force networks in granular systems [20]. For example, Luding [17] used the DEM to investigate how the spatial stress distribution changes if polydispersity is introduced into packings of disks organized in a perfectly hexagonal lattice. For exactly monodisperse particle packings, particle stresses are distributed uniformly, in agreement with the hypothesis of Liu *et al.* [5]. However, as soon as polydispersity is introduced by varying the diameter (as little as $\pm 0.33\%$ of the mean diameter) a heterogeneous stress distribution, i.e., the occurrence of force chains, was observed [17]. Both experimental and numerical works [5,17] have established a link between the packing morphology and the contact force distribution in packings of spherical particles. However, thus far, this link has not been investigated for nonspherical particles.

Among the nonspherical particle packings studied, those composed of highly nonconvex particles are particularly interesting as nonconvex particles can interlock, forming packings that may sustain compressive and tensile forces despite containing purely noncohesive particles [13,21,22]. Owing to these particular characteristics, packings of highly nonconvex, interlocking particles may find practical relevance, for example, in architecture by enabling novel construction concepts such as aleatory construction [21,23–25]. However, despite their intriguing characteristics, so far, only a few studies have investigated the distribution of contact forces, $P(f)$, in packings composed of nonspherical particles. For example, Gan *et al.* [26] performed 3D DEM simulations of packings of oblate ellipsoids with their sphericity (Ψ) varying between 1 and 0.7. Interestingly, the $P(f)$ for ellipsoids was similar to

the distribution of spheres; i.e., $P(f)$ peaks close to $f = 1$ and for $f > 1$ $P(f)$, decays exponentially (type A distribution). The exponential decay was fitted by Eq. (2) with k ranging between 1.2 and 1.4 depending on particle sphericity. However, there did not seem to be a clear correlation between the sphericity of the particles and the exponent k characterizing the decay. Similar results were reported by Saint-Cyr *et al.* [14] who simulated compressed packings of particle clusters composed of three disks glued together in a triangular arrangement (trimers). The sphericity of the trimer particles was varied between 1 and 0.76 by varying the overlap of the trimer particles. A key finding of their work was that in compressed packings of trimers, $P(f)$ resembles the distribution of spheres (type A) with an exponential decay (for $f > 1$) with $k = 1.7$, independent of the particle sphericity, hence confirming the results of Gan *et al.* [26]. When the compressed trimer particles were also sheared (instead of only compressed), k decreased with decreasing sphericity (Ψ), i.e., k reduced from 1.7 to 1 for Ψ decreasing from 1 to 0.76. The behavior of the reference case (disks with $\Psi = 1$) was different in that $P(f)$ was not affected by the addition of shear. Furthermore, Saint-Cyr *et al.* [14] showed that in sheared packings of spheres, the shape of $P(f)$ is concave and resembles a type A distribution. However, for nonspherical particles with $\Psi < 0.96$, $P(f)$ increases for $f \rightarrow 0$, leading to a type B distribution without a peak. Further, it was found that $\lim_{f \rightarrow 0} P(f)$ increased with decreasing sphericity. The decreasing value of k for decreasing particle sphericity and the absence of a peak at $f \approx 1$ leads to the key conclusion that in sheared packings $P(f)$ becomes increasingly heterogeneous for decreasing sphericity. The results of Saint-Cyr *et al.* were confirmed by Azéma and Radjai [15] in 2D simulations of sheared, half-disk-capped rectangular particles which resemble 2D spherocylinders. Azéma and Radjai [15] varied the sphericity of the particles from 1 to 0.82 and found the exponent k in $P(f) = e^{-kf}$ to decrease from 1.8 to 0.85, respectively. Moreover, they could also confirm that for particles with $\Psi < 0.99$, $P(f)$ resembles a type B distribution where $\lim_{f \rightarrow 0} P(f)$ increased for decreasing Ψ . Highly nonconvex particles of very low sphericity ($\Psi = 0.45$) (and spheres as a reference case) were studied by Murphy *et al.* [13]. The objective of their work was to find particle shapes that can form freestanding, externally unconfined packings that can support load (i.e., searching for packings of interlocking particles that can sustain compressive and tensile stresses). Particles of low sphericity were modeled by gluing together multiple spheres to yield Z-shaped particles. For the reference case, a 3D compressed packing of spheres, the well-established type A contact force distribution was observed, with a decay exponent of $k = 1.4$. However, compressed 3D packings of Z-shaped particles have a force distribution of type B, similar to the distributions observed by Saint-Cyr *et al.* [14] and Azéma and Radjai [15] in 2D sheared packings of nonspherical particles ($0.96 > \Psi > 0.76$). Additionally, the contact force distribution of Z-shaped particles ($\Psi = 0.45$) had a very long exponential tail with an exponent k ranging between 0.56 and 0.76 depending on the specific Z shape.

From the above, one can conclude that in sheared 2D packings the exponential tail of the contact force distribution, $P(f)$, becomes longer with increasing particle nonsphericity,

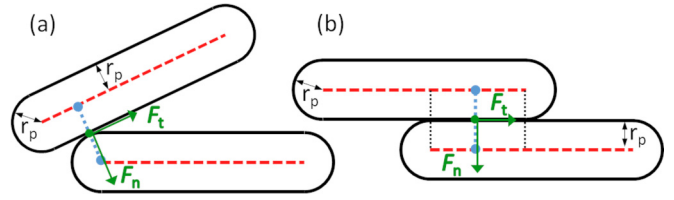


FIG. 2. Schematic of two contacting spherocylinders. The red dashed lines denote the central axis of each spherocylinder. The spherocylinder radius is labeled r_p . The blue dotted line depicts the shortest distance between the central axis of the two spherocylinders. F_n and F_t depict the normal and tangential forces acting at the contact point (green): (a) contact between a cylindrical section and a hemispherical end cap; (b) parallel contact between spherocylinders.

i.e., k decreases with decreasing Ψ . In addition the shape of $P(f)$ transitions from a type A shape to a type B upon shearing [14,15]. However, in compressed 2D packings a decrease of k , as well as a change from a type A to type B distribution, with increasing particle nonsphericity does not occur for particles with $\Psi > 0.76$. Conversely, in compressed 3D packings of particles with $\Psi = 0.45$ a type B force distribution with $k \leq 0.76$ was observed. Hence, it still remains unclear whether (i) contact force distributions of type A prevail in compressed 2D packings of particles of low sphericity ($\Psi < 0.76$) and (ii) the contact force distribution of low-sphericity particles ($\Psi < 0.76$) changes from a type A to type B distribution when transitioning from 2D to 3D packings.

In this work we address these two questions to establish a general correlation between particle sphericity and the shape of the contact force distribution in compressed 2D and 3D packings of nonspherical particles. While 2D packings do not occur in nature they are frequently studied, in particular experimentally. To allow a comparison between the results of this work and previous experimental 2D and numerical 3D studies, packings of various dimensionality are studied here. In addition, we probe whether the conclusion drawn by Liu *et al.* [5] and Luding [17] for spherical particles, viz., that a more heterogeneous packing morphology leads to a longer exponential tail in the distribution function of the contact force, can be extended to nonspherical particle packings.

II. METHODS

The DEM algorithm used in this study is a modification of the original concept proposed by Cundall and Strack which was developed for disk-shaped particles [20]. The present work considers particles that are created by combining multiple spherocylinders (cylinders with hemispherically capped ends), analogous to the commonly applied glued-sphere approach [27]. A spherocylinder is a computationally benevolent particle shape since all points on its surface have the same distance from the central axis (see Fig. 2). The general concept used in the DEM to track particles and particle contacts has been well documented in the literature [20,27–32]. Hence, the following will only describe the contact model and the contact detection algorithm between spherocylinders.

A. Particle contacts

Since all points on the surface of a spherocylinder have the same distance from the central axis (red dashed line in Fig. 2), the contact detection for spherocylinders can be reduced to the task of finding the closest points between two line segments. We solve this task using the algorithm proposed by Lumelsky [33]. The point at which the contact forces act is called the contact point and corresponds to the center point (green point in Fig. 2) of the line that connects the two closest points on each of the central axes (blue line in Fig. 2). The normal contact force (F_n in Fig. 2) acts perpendicular to the surface of the particle, while the tangential force (F_t), resulting from friction, acts parallel to the surface. The direction in which the tangential force acts depends on the relative velocity of the particles at the contact point and the accumulated displacement between the particles.

If the angle between the central axes of the two contacting spherocylinders is less than 2° , the contact is treated as a parallel contact [Figure 2(b)]. The value of 2° is chosen as a feasible and efficient cutoff value based on additional numerical experiments. These experiments demonstrated that varying the cutoff angle between 0.01° and 5° does not affect the packing density nor the particle orientations. For a parallel contact, the middle of the parallel sections that align is chosen as the contact point [Figure 2(b)].

The contact between two particles is modeled by a linear spring dashpot. The linear spring dashpot model leads to a constant coefficient of restitution, independent of the collision velocity [34]. A linear model instead of a more realistic nonlinear Hertzian model is justified as previous works have shown that packings of spherocylinders, when using either linear or Hertzian contact models, did not differ in the probability distribution of the contact forces [35]. It has also been argued that the material stiffness should increase with increasing contact area, e.g., in the case of a parallel contact between two spherocylinders [Fig. 2(b)] [36–38]. However, a recent study has shown that varying the contact stiffness in the case of parallel contacts has little influence on the force distribution and structure in packings of spherocylinders [35]. Consequently, in this work, the normal and tangential stiffness are assumed to be constant, regardless of the geometry of the contact.

The contact force in the normal direction, F_n , between two contacting particles i and j is

$$F_n = \max\left(0, \frac{k_n}{2}\delta_n - \eta_n\sqrt{2m_{ij}k_nv_n}\right). \quad (3)$$

Here k_n is the normal stiffness of the particles, δ_n is the overlap between the contacting particles, η_n is the damping factor in the normal direction, and v_n is the normal component of the relative velocity between the particles at the point of contact. The effective inertial mass m_{ij} is calculated by

$$m_{ij} = \frac{m_im_j}{m_i + m_j}. \quad (4)$$

In the tangential direction (subscript t), the maximal contact force is limited by Coulomb's law of friction and is calculated

by

$$F_t = \min\left(\mu\frac{k_n}{2}\delta_n, \frac{k_t}{2}\delta_t - \eta_t\sqrt{2m_{ij}k_tv_t}\right), \quad (5)$$

where μ is the coefficient of friction, η_t is the tangential damping factor, k_t is the tangential stiffness, and v_t is the tangential component of the relative velocity between the particles at the point of contact. The accumulated tangential displacement at the contact is calculated as $\delta_t = \int v_t dt$.

B. Simulation parameters

The density of the particles is fixed to $\rho = 1000 \text{ kg/m}^3$ which is close to the density of many plastics, e.g., polyethylene (PE) or acrylonitrile butadiene styrene (ABS). Such plastics are commonly used in manufacturing techniques such as injection molding or fused deposition modeling, which can be employed to manufacture nonspherical particles. To choose a value for the normal particle stiffness k_n two competing factors have to be considered: One factor is that a decreasing k_n leads to a larger time step dt which decreases the computational time. As a rule of thumb dt should be at least 20 times smaller than the duration of a collision t_{col} which can be approximated by a damped harmonic oscillator [39]:

$$t_{\text{col}} = \frac{\pi}{\sqrt{\frac{k_n}{m_{ij}}(1 - \eta_n^2)}}. \quad (6)$$

Furthermore, particles in a packing experience the weight of the particles above them which can lead to a vertical gradient of the magnitude of the contact forces. The influence of this gradient on the contact force probability distribution needs to be considered. Some researchers have eliminated the influence of this gradient by normalizing the contact forces by the weight of the particles above a given depth in the packing [5]. In our work a different approach is used to eliminate the effect of the vertical gradient in the magnitude of the contact forces, which is by exerting an additional vertical load onto the packing through a forced compression at the top. If the contact forces due to the external compression are sufficiently high, the influence of the vertical gradient can be neglected. However, increasing the contact force between particles, without changing the stiffness, increases the overlap δ_n between the particles which can lead to computational stability problems. Hence, a sufficiently high k_n is desired to be able to neglect the vertical gradient in the magnitude of the contact forces. For the given particle density of $\rho = 1000 \text{ kg/m}^3$ an external compression force of 500 N was found, through simulations, to be sufficient to eliminate the influence of the vertical gradient in the magnitude of the contact forces. For an external compression force of 500 N a normal particle stiffness k_n of 100 000 N/m is required to limit the particle overlaps to $\delta_n < 0.05 d_p$, where d_p is the spherocylinder diameter. Additional simulation results show that increasing k_n by an order of magnitude does not influence the contact force distributions; decreasing k_n by an order of magnitude while keeping the compression force constant leads to unstable simulations. In conclusion, any set of values for the parameters ρ , k_n , dt , and the compression force can be chosen, without affecting

TABLE I. Material parameters used in the simulations.

Parameter	Symbol	Value
Density	ρ	1000 kg/m ³
Normal stiffness	k_n	100000 N/m
Tangential stiffness	k_t	50000 N/m
Coefficient of restitution	ε	0.53
Normal damping factor	η_n	0.2
Tangential damping factor	η_t	0.2
Coefficient of friction	μ	0.5
Wall friction coefficient	μ_w	0
Spherocylinder diameter	d_p	0.005 m
Time step	dt	2×10^{-6} 1/s

the results, as long as the set satisfies the conditions outlined above.

The damping factor in the normal direction η_n is assumed to be constant and is related to the coefficient of restitution ε via

$$\varepsilon = \exp\left(\frac{-\pi \eta_n}{\sqrt{1 - \eta_n^2}}\right). \quad (7)$$

In this work, $\varepsilon = 0.53$ ($\eta_n = 0.2$) is chosen as previous studies have shown that varying ε in the range 0.2–0.9 has little influence on the behavior of dynamic granular systems such as rotating drums and flows down an inclined plane [40,41]. We expect the influence of ε on the results of a static granular packing to be even less significant than for dynamic systems. For the tangential stiffness $k_t = 0.5 k_n$ is chosen in accordance with previous works [30,31,42], while for the friction coefficient a value of $\mu = 0.5$ is chosen. A discussion about the influence of particle friction on the contact force probability distribution can be found in the Supplemental Material [43].

Friction at the domain walls is neglected by setting the coefficient of friction between particles and the domain walls to $\mu_w = 0$, as some authors [44] have argued that friction between particles and the domain wall leads to a more heterogeneous particle packing. The influence of a frictional wall on a packing is most pronounced close to the wall. In the work reported here, the dimensionality of the domain is varied. Hence, to isolate the effect of dimensionality on a particle packing, the effect of wall friction has to be eliminated. Furthermore, other numerical works on nonspherical particles [13,14] have also chosen to neglect wall friction. For these reasons wall friction is also neglected in this work. Of course, frictionless walls are typically not observed in experiments. To aid comparison with experimental work the influence of the wall friction on the particle packing is discussed in the Supplemental Material [43].

Table I summarizes the values of the parameters used in the simulations. The value of the parameters of the confining walls are identical to those of the particles, except for the friction coefficient.

C. Cluster particles

The combination of several spherocylinders to spherocylinder-cluster particles, analogous to the glued-

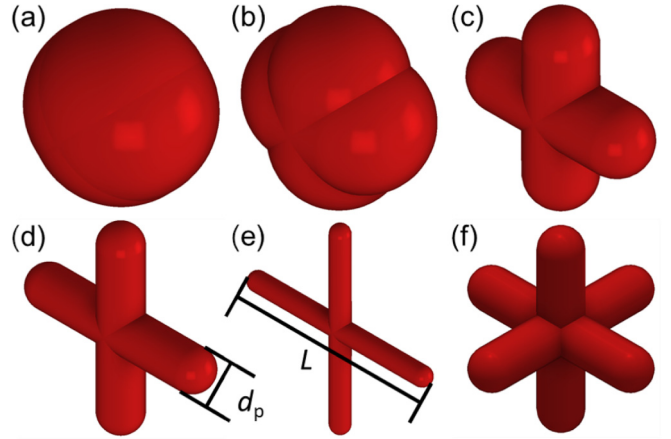


FIG. 3. Selection of cross- and star-shaped particle geometries with varying sphericities (Ψ): (a) Cross-shaped particle with $\Psi = 0.99$, (b) cross-shaped particle with $\Psi = 0.96$, (c) cross-shaped particle with $\Psi = 0.75$, (d) cross-shaped particle with $\Psi = 0.59$, (e) cross-shaped particle with $\Psi = 0.47$, and (f) star-shaped particle with $\Psi = 0.53$.

sphere approach [27,37], does not require additional contact detection routines [27]. The contact between two cluster particles can be treated as a contact between individual spherocylinders. The contact forces acting on the different spherocylinders belonging to a cluster are summed up and act on the center of gravity of the cluster.

In this study, two different types of cluster particles are investigated. In 2D packings, cross-shaped particles are used [Figs. 3(a)–3(e)]. Cross-shaped particles are formed by intersecting two perpendicular spherocylinders of equal length in their centers. In simulations of pseudo-2D and -3D packings, star-shaped particles (also referred to as jacks or hexapods) are used. Such particles are formed by intersecting a cross-shaped particle with a third spherocylinder (of the same length) perpendicular to both spherocylinders that form the cross [Fig. 3(f)]. These particle shapes are chosen as they model nonconvex geometries with a high order of symmetry and are easy to construct.

The nonconvexity of cross- and star-shaped particles increases with decreasing sphericity (Ψ). Various definitions for sphericity have been proposed [45–47], whereby the most common definition is the ratio of the surface area of a sphere to the surface area of a nonspherical particle with the same volume as the sphere [46,48,49]. The present work uses this definition and thus for a sphere $\Psi = 1$ and for nonconvex particles $\Psi < 1$. The sphericity of the particle shapes modeled in this work ranges from $\Psi = 0.99$ to 0.42, hence covering a broad range of shapes from almost spherelike to very slender highly nonconvex shapes [Fig. 3(e)].

Some authors [50,51] have argued that several parameters, such as sphericity, blockiness, and convexity, have to be specified to distinguish between different nonspherical particle shapes. We agree with the general rationale behind this proposal; however, this work investigates only two different shapes of particles, i.e., cross-shaped and star-shaped particles. For these two particle shapes any nonsphericity-describing parameter, e.g., blockiness or convexity, scales

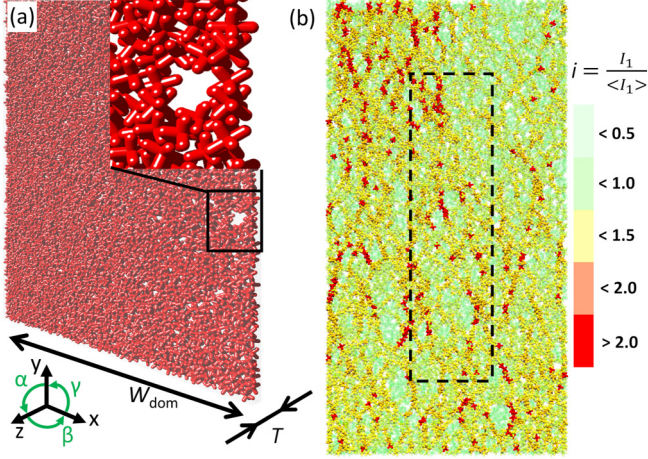


FIG. 4. (a) Visualization of a pseudo-2D packing of star-shaped particles ($\Psi = 0.619$) with $W_{\text{dom}} = 30L$ and $T = L$ (L = particle length). (b) Visualization of the normalized, first stress invariant ($i = I_{1,i} / \langle I_1 \rangle$) of the packing shown in (a). The dashed area depicts the area that is used to calculate the radial distribution function (RDF). The results of the RDF are shown in Fig. 7.

monotonically with (non-)sphericity. We believe that due to this monotonic scaling, the introduction of a second nonsphericity parameter would be redundant, provided that particles of one shape are compared only to particles of the same shape (as is the case of this study). An exception is made for the particle aspect ratio [defined as the ratio of the overall length of a particle L to the diameter of the protruding arms d_p (Fig. 3)] which was used by other works [21,22] to describe star-shaped particles. To aid the comparison between our work and the works reported in Refs. [21,22] the relationship between the particle aspect ratio and the particle sphericity is given in the Supplemental Material [43].

D. Simulation domains

Four different domain configurations (defined by the confining walls) are assessed in this work: (i) 2D simulations in which cross-shaped particles cannot move in the z direction (coordinate system shown in Fig. 4). In these 2D simulations the domain width W_{dom} (x direction) is equal to 30 times the particle length L . Therefore, W_{dom} changes with particle shape Ψ ; (ii) pseudo-2D simulations in a cuboidal domain with a transverse thickness T (z direction) equal to L . As in the 2D simulations, $W_{\text{dom}} = 30L$; (iii) pseudo-2D simulations in a cuboidal domain with $T = 2L$ and $W_{\text{dom}} = 30L$; and (iv) 3D simulations in a cylindrical domain of diameter $D_d = 10L$. A visualization of the pseudo-2D simulation with $T = 2L$ is given in Fig. 4(a).

For 3D domains two diameters D_d are investigated, i.e., $D_d = 6L$ and $D_d = 10L$; for these two domain sizes very similar results are obtained for the contact force distributions. To have a larger data set for the contact force distributions, the results of the larger 3D domain ($D_d = 10L$) are presented in the following. For the pseudo-2D domain, a transverse thickness of $T = L$ is chosen; this thickness is as close as possible to a 2D domain while still allowing rotations around any given axis of the star-shaped particles. To investigate how

a change in the transverse thickness affects the structure of the packing and transmission of contact forces, pseudo-2D domains with $T = 2L$ are simulated. As the results of the pseudo-2D domains with $T = 2L$ are similar to the 3D results, T is not increased further.

To initialize a simulation, the domain is filled by placing all of the particles on a regular lattice with a space of $1.5d_p$ between each particle. The height of the simulation domain (y direction) is chosen just large enough to accommodate all of the particles in the initialization lattice. The particles are initialized with a random rotational orientation and a random velocity v ($-0.25 \text{ m/s} < v < 0.25 \text{ m/s}$) in the y and z directions (2D and $T = L$ cases) or a random velocity in all three directions (3D and $T = 2L$ cases). The particles are allowed to settle for a time $t_{\text{settle}} = 3\sqrt{\frac{2h}{g}}$, where g is the acceleration due to gravity and h is the domain height. After time t_{settle} , the particles have come to rest as the average displacement of the particles per time step approaches numeric precision. Once the particles have settled, the domain is compressed by moving a planar wall from the top downward with a speed of 0.25 m/s until the packing exerts the external compression force of 500 N onto the top wall. This procedure simulates the uniaxial compression of a granular material in a container with rigid walls.

The number of particles in each simulation N is such that the height of the packing (after compression) is at least twice as high as W_{dom} (or in the case of a cylindrical domain the diameter of the cylinder). In the different configurations N ranges from 1800 to 34 500.

To avoid crystallization at low values of Ψ , a particle size distribution is introduced. In 2D simulations, the polydispersity factor (by which the particle size is scaled) is ± 0.3 for $\Psi > 0.88$, and ± 0.15 for $0.88 \geq \Psi > 0.75$. For pseudo-2D and -3D simulations, the polydispersity factor is ± 0.2 for $\Psi > 0.86$. As reference cases, packings of spherical particles (diameter $d_p = 0.005 \text{ m}$, polydispersity factor ± 0.2) in a 2D domain with $W_{\text{dom}} = 30d_p$ and in a cylindrical domain with a cylinder diameter of $10d_p$ are simulated.

E. Data analysis: Contact forces, stress analysis, and packing structure

Previous studies using spherical particles typically focused on the normal component of the contact force [12–14]. Thus, we likewise report here the distribution of the normal contact forces. For the computation of the probability distribution of the contact forces, $P(f)$, the normalized forces f are sorted into 50 bins of size 0.2 (range 0–10).

Particle stresses are obtained by calculating first the stress tensor of the individual particles according to [52]

$$\bar{\sigma} = \frac{1}{V} \begin{bmatrix} \sigma_{xx} & \sigma_{xy} & \sigma_{xz} \\ \sigma_{yx} & \sigma_{yy} & \sigma_{yz} \\ \sigma_{zx} & \sigma_{zy} & \sigma_{zz} \end{bmatrix} = \frac{1}{V} \sum_c \bar{F}_{n+t}^c \bar{r}^c, \quad (8)$$

where V is the particle volume, c is the number of all particle contacts, \bar{F}_{n+t} is the sum of the normal contact force and the tangential contact force, and \bar{r} is the vector pointing from the center of the particle to its contact point. The particle stress tensor is diagonalized to obtain the principal stresses.

Additionally, this work reports the sum of the elements of the diagonalized stress matrix (trace) of each particle, i.e., the first stress invariant of the tensor for each particle ($I_{1,i}$). Similar to the presentation of the contact forces $I_{1,i}$ is normalized by its mean ($\langle I_1 \rangle = \frac{1}{N} \sum_i I_{1,i}$) yielding $i = I_{1,i}/\langle I_1 \rangle$.

The packing morphology is analyzed by calculating the radial distribution function (RDF) which is given by Eq. (9). The RDF can be interpreted as the number of particles that are located in a differential volume shell (thickness Δr) with a distance r from the particle center, divided by the expected number of particles based on the particle number density of the whole packing. Here the center of mass of a cross- or star-shaped particle is considered as the particle center. The RDF plots show $G(r)$ over r/L , where r has been normalized by the respective particle length L .

$$G(r) = \frac{N_{\text{RDF}}(r)}{4r^2 \Delta r N \rho_N}. \quad (9)$$

In Eq. (9) ρ_N is the average number density of the particles (number of particles in the simulation domain divided its volume) and N_{RDF} is the number of particles in the differential volume shell given by

$$N_{\text{RDF}} = \sum_i \sum_{j \neq i}^{N_{10L}} \delta(r - r_{ij}), \quad (10)$$

where δ is the Dirac delta function, r_{ij} is the distance between the center of particle i to the center of particle j , and N_{10L} is the number of particles which have a distance of at least $10L$ from each side wall as well as the top and bottom of the 2D domain. This area is sketched in Fig. 4(b). In the 3D case, N_{10L} corresponds to the number of particles that have at least a distance of $10L$ from the top and bottom wall and a distance of $3L$ from the cylinder wall. We exclude particles close to the wall because these particles have no close neighbors outside of the walls.

III. RESULTS

A. Contact force distributions

As a first approach, we assess whether our simulations support a previously reported trend that the exponential tail of $P(f)$ becomes longer for increasingly nonspherical particles [13–15,26]. Currently, it is unclear whether such a trend is limited to a given domain dimensionality (2D vs 3D) and whether compressed packings show the same behavior as sheared systems. Figure 5 plots the probability distributions of the normal contact forces normalized by their mean, $P(f)$, for different particle sphericities and domain configurations.

For 2D domains, the $P(f)$'s of cross-shaped particles with the highest investigated sphericity ($\Psi = 0.995$) and spheres are very similar [Fig. 5(a)]. In 2D packings, changes in the $P(f)$ when transitioning from packings of spherical particles to slightly nonspherical particles seem to occur gradually. Figure 5(a) also plots Eq. (1), the numerical expression for $P(f)$ proposed by Mueth *et al.* [12]. Somewhat surprisingly, the empirical equation (1), although extracted originally from a packing of spheres, agrees well with the data for low-sphericity cross-shaped particles in 2D, but not with the simulation results of spheres. A possible reason for this de-

viation might be the fact that Mueth *et al.* [12] studied 3D packings and only recorded contact forces at the wall. Indeed, the numerical results of a packing of spheres in a 3D domain, Fig. 5(d), agree very well with Eq. (1).

When comparing the contact force distribution, $P(f)$, of cross-shaped particles (2D domain) as a function of their sphericity [Fig. 5(a)], one can observe that the length of the exponential tail of $P(f)$ increases with decreasing Ψ . However, the increase in the length of the exponential tail is limited. Even in packings of cross-shaped particles with a sphericity of $\Psi = 0.473$ (lowest sphericity modeled) only four individual contact forces (out of 10^5) have a value of $f > 8$. The general type A shape of the distributions, i.e., a peak at $f \approx 1$ and an exponential tail, is independent of particle sphericity when the packing is restricted to 2D. Hence, our results confirm the observations by Saint-Cyr *et al.* [14] who modeled trimers ($1 \geq \Psi \geq 0.76$) and observed that the shape of $P(f)$ and the location of its peak is independent of particle sphericity in compressed 2D packings.

Turning now to pseudo-2D packings of star-shaped particles [Figs. 5(b) and 5(c) for, respectively, $T = L$ and $T = 2L$], one observes a change in the shape of $P(f)$ from type A to type B with decreasing particle sphericity. Generally, the peak at $f \approx 1$ becomes less pronounced and the length of the exponential tail increases with decreasing sphericity. Only for particles with the highest sphericity ($\Psi = 0.995$) the shape of $P(f)$ in pseudo-2D packings coincides with the shape that is observed in 2D simulations.

When increasing the transverse thickness of the pseudo-2D simulations [$T = 2L$, Fig. 5(c)] and ultimately reaching full 3D simulations, Fig. 5(d), the shape of $P(f)$ changes further; i.e., the peak of $P(f)$ remains at $f \approx 1$ for high-sphericity particles but is no longer visible for low-sphericity particles ($\Psi = 0.461$ and $\Psi = 0.419$). Furthermore, the length of the exponential tail increases significantly for $\Psi < 0.7$ when increasing the transverse thickness of the domain to $T = 2L$ and 3D. It has been suggested that type A distributions are essentially Gaussian-like (centered around $f \approx 1$, albeit truncated at $f = 0$) which would indicate that the forces are distributed homogeneously [13,18]. The similarity between a type A distribution and a Gaussian-shaped distribution is shown in Fig. 1. One can see that a Gaussian is a good fit for type A distributions for $f < 3$, but the type A distribution has a longer tail. On the other hand, the lack of a peak at $f \approx 1$ and the long exponential tails of type B distributions represent a heterogeneous force distribution with a large number of below-average contact forces but also some contact forces that are ten times above average.

To summarize, our results show that in pseudo-2D and -3D packings the shape of $P(f)$ changes from type A to type B when the particle sphericity decreases below the critical value $\Psi_{\text{crit}} = 0.7$ (but not in 2D packings). The shape change comes with an increasing length of the exponential tail of $P(f)$ and a decreasing prominence of the peak at $f \approx 1$ with decreasing particle sphericity. Our results establish a connection between the observations of several previous studies: Saint-Cyr *et al.* [14] and Azéma and Radjai [15] who observed exclusively type A distributions in compressed 2D packings of nonspherical particles.

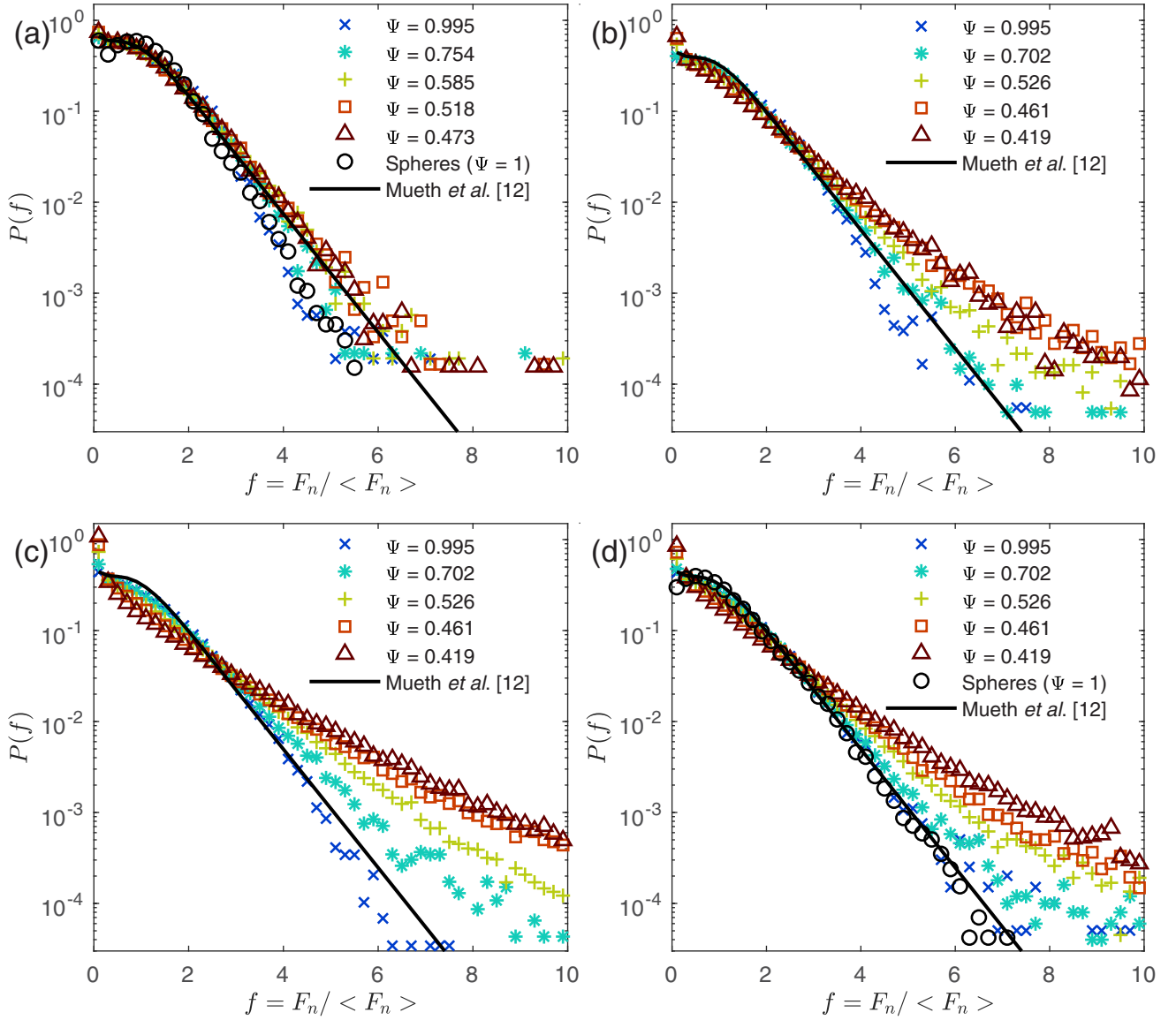


FIG. 5. Probability distribution functions, $P(f)$, of the normal contact force (F_n) normalized by the mean normal contact force [$\langle F_n \rangle$] for all four packing domains simulated. In the 2D domain (a) the flat, cross-shaped particles can only translate in the x and y directions. In the pseudo-2D domains (b) three-dimensional particles can translate in all three directions, with the transversal domain width T in the z direction being as large as the particles ($T = L$). In the second pseudo-2D domain (c) the z direction is twice as large as the particles ($T = 2L$). The 3D domain (d) is cylindrical with diameter $D_d = 10L$. For each packing configuration the full range of particle sphericities simulated is shown. For reference a 2D simulation of spheres is included in (a) and a 3D simulation of spheres is included in (d). Each panel also plots the probability distribution function predicted by the empirical equation [Eq. (1)] of Mueth *et al.* [12], which was derived from compressed 3D packings of glass spheres.

On the other hand, Gan *et al.* [26] who simulated ellipsoids with $\Psi \geq 0.7$ in 3D packings, observed type A distributions and Murphy *et al.* [13] who simulated Z-shaped particles with $\Psi = 0.45$ in 3D packings observed type B distributions.

Combining the results of our simulations with previously reported observations allows us to draw the following general conclusion for the shape of $P(f)$ in 2D and 3D packings of compressed nonspherical particles with different shapes and sphericities:

(1) With decreasing particle sphericity, the contact force distribution of compressed 3D packings becomes more heterogeneous. This is evidenced by the increasing length of the

exponential tail of the contact force distribution with decreasing particle sphericity for $\Psi < \Psi_{\text{crit}} = 0.7$, independent of the specific particle shape.

(2) In compressed 2D packings the length of the exponential tail of the contact force distributions does not depend on particle sphericity.

B. Quantification of the length of the exponential tail

Next, a quantitative description of the length of the exponential tail is explored. In the following, we will focus on the region $f > 1$ of $P(f)$, due to the importance of the large

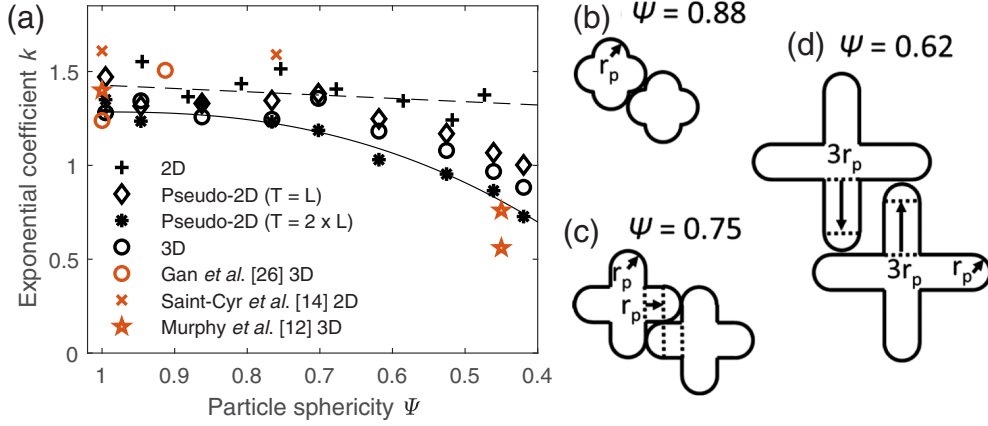


FIG. 6. (a) Exponent k [Eq. (2)] obtained by fitting the exponential tail ($f > 1$) of the contact force distributions. Results of the present work are shown by black markers, while red markers denote results from previously published studies. The dashed line is a linear fit [$k(\Psi) = 0.18(1-\Psi) + 1.43$] to the values of k obtained in 2D packings (+), while the solid line is an exponential fit [$k(\Psi) = -2.03(1-\Psi)^{2.43} + 1.29$] to the values of k obtained in pseudo-2D ($T = 2L$) packings (*). (b)–(d) Sketches of cross-shaped particles showing how the lengths of the protruding arms change with sphericity.

forces which can potentially lead to the fracture of particles and endanger a stable packing.

Figure 6(a) plots the exponent k as a function of particle sphericity. The exponent k is obtained by fitting the exponential tail ($f > 1$) of the different $P(f)$'s (Fig. 5) with Eq. (2). Error bars are omitted in Fig. 6(a) for clarity (the 95% confidence bounds for k are typically within ± 0.025). Qualitatively the homogeneity of $P(f)$ decreases as the length of the tail increases (i.e., a lower value of k).

For particles of high sphericity ($\Psi = 0.995$), the values obtained for k are in the range $1.28 \geq k \geq 1.47$. These values are in between the values obtained by Mueth *et al.* [12] (packings of glass spheres in 3D with $k = 1.5$) and Gan *et al.* [26] (3D packing of spheres with $k = 1.24$).

Turning now to less spherical particles: In 2D packings, k decreases slightly with decreasing Ψ , i.e., $k = 1.42$ for $\Psi = 0.995$ and $k = 1.32$ for $\Psi = 0.47$. In 2D packing the decrease of k with decreasing Ψ can be fitted well by a linear function (dashed black line in Fig. 6(a)). The comparatively high value of $k = 1.32$ for the lowest sphericity values studied ($\Psi = 0.47$) shows that there are relatively few cases of high-contact forces in 2D packing of low-sphericity particles. Good agreement is also seen when including data for k obtained by other works that have assessed compressed 2D packings (e.g., the data of Saint-Cyr *et al.* [14] are for trimer particles).

In pseudo-2D and -3D packings $k = 1.38 \pm 0.14$ for $\Psi > \Psi_{\text{crit}} = 0.7$. For $\Psi < \Psi_{\text{crit}}$ k decreases exponentially with decreasing Ψ and reaches a value of $k = 0.87 \pm 0.13$ for the lowest sphericity investigated, i.e., $\Psi = 0.42$. An exponential fit of k in pseudo-2D ($T = 2L$) packings is shown by a solid line in Fig. 6(a). Hence, for $\Psi < \Psi_{\text{crit}}$ the probability of finding large contact forces ($f > 8$) increases exponentially and the contact force distributions become increasingly heterogeneous. The critical sphericity value, i.e., $\Psi_{\text{crit}} = 0.75$ for cross-shaped particles (2D) and $\Psi_{\text{crit}} = 0.7$ for star-shaped particles (3D) is the lowest sphericity for which a contact between two particles always involves the hemispherically capped ends of the particles. This can be explained by the fact that at this critical sphericity the arms protruding from

a particle are exactly twice as long as the particle radius [Fig. 6(c)]. For $\Psi > \Psi_{\text{crit}}$, contacts will always involve the end caps of a particle [Fig. 6(b)], while for $\Psi < \Psi_{\text{crit}}$, contacts can also involve the flat or cylindrical section of the protruding arms [Fig. 6(c)]. Particles that only contact each other with the hemispherical end caps, i.e., star-shaped particles with $\Psi \geq 0.7$, are more likely to slip relative to each other when a load is applied. Conversely, particles with contacts that involve the flat/cylindrical sections of the arms, i.e., star-shaped particles with $\Psi < 0.7$, are less likely to slip relative to each other which means that they are more likely to jam. When a particle jams during compression, the contact forces acting on such a particle can increase substantially (and without the particle unjamming the contact forces cannot relax). These high contact forces give rise to the long exponential tail of $P(f)$ for low-sphericity particles, in particular for star-shaped particles with $\Psi < 0.7$. Whereas this rationale explains the transition at $\Psi_{\text{crit}} = 0.7$ for pseudo-2D and -3D packings, it is unclear why such a pronounced transition is absent for 2D packings. We speculate that the reason might lie in the particular spatial distribution (morphology) of the particles which will be investigated in the following.

C. Packing morphology

By analyzing the probability distribution of the contact forces, $P(f)$, we found that in compressed pseudo-2D and -3D particle packings the length of the exponential tail of $P(f)$ increases with decreasing particle sphericity. In contrast, in 2D packings, the length of the exponential tail of $P(f)$ does not depend strongly on the particle sphericity. Hence, the question why the behavior of 3D packings differs distinctively from 2D packings remains unanswered. Instead of assessing the structure of a packing by an averaged, global parameter, such as the solid fraction, the morphology of the packings is assessed by calculating their radial distribution functions, RDF [$G(r)$, Fig. 7].

Comparing the RDFs in 2D packings as a function of sphericity [Fig. 7(a)], one observes that for cross-shaped par-

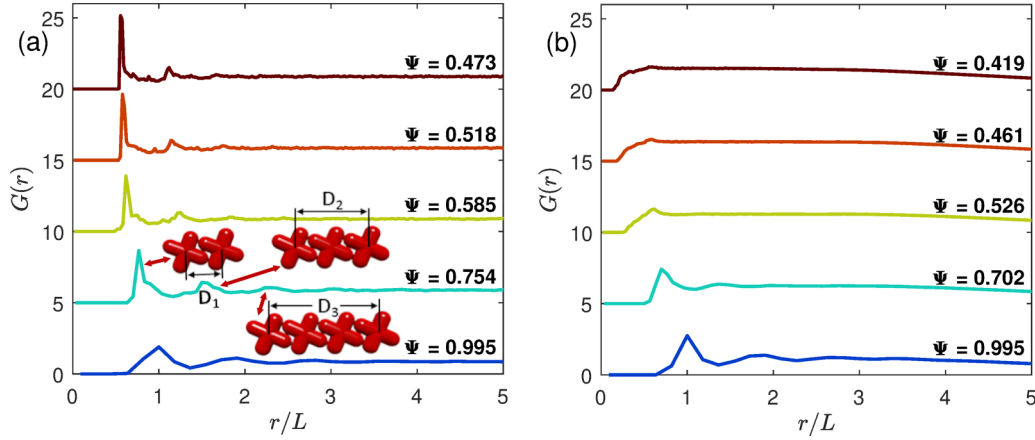


FIG. 7. Radial distribution function (RDF), $G(r)$, for (a) 2D and (b) 3D packings of particles of different sphericity. For better readability, the curves are shifted vertically with an offset of 5. In 2D packings, the distance between the particle centers corresponding to the first, second, and third peaks are labeled D_1 , D_2 , and D_3 . The distances D_1 – D_3 can be determined analytically according to Eq. (11), and J_1 according to Eq. (12).

ticles of low sphericity ($\Psi = 0.75$) the first ($r/L = 0.76$) and second ($r/L = 1.5$) peaks are more prominent compared to the first ($r/L = 1$) and second ($r/L = 1.91$) peaks of more spherical particles ($\Psi = 0.995$). These peaks correspond to particle configurations of local crystallinity which are also the closest possible arrangements of interlocking particles. Sketches of such crystalline particle configurations are shown in Fig. 7 (and enhanced in the Supplemental Material [43]). More pronounced peaks imply a more frequent occurrence of the respective particle configurations. The distances D_1 , D_2 , D_3 between the centers of two interlocking particles, as defined in Fig. 7, can be calculated by

$$D_1 = \sqrt{d_p^2 + [(L + d_p)/2]^2}, \quad D_2 = 2D_1, \quad D_3 = 3D_1. \quad (11)$$

For cross-shaped particles with $\Psi = 0.75$ the values of the first ($r/L = 0.76$) and second ($r/L = 1.5$) peaks of the RDF are close to the geometrically determined values of the D_1 and D_2 configurations ($D_1/L = 0.75$ and $D_2/L = 1.49$). This indicates that the peaks in the RDF indeed correspond to the proposed closest crystalline configurations. In the RDF of 2D packings of particles with $\Psi = 0.75$ the peak positions are shifted to lower values of r/L compared to the RDF of 2D packings of more spherical particles ($\Psi = 0.995$). The position of the peaks (D_1/L) shifts to lower values for decreasing Ψ because L increases with decreasing Ψ and $\frac{D_1}{L} \propto \frac{(L + \sqrt{L})}{2L} < 1$. For 2D packings of cross-shaped particles with $\Psi = 0.75$ a small third peak can be seen at $r/L = 2.23$, which corresponds to a similar packing configuration as the one described above (four-particle configuration) with an analytical value of $D_3/L = 2.24$. These first three peaks can also be seen in the RDFs of 2D packings of particles with lower sphericity. The positions of the peaks as well as the analytically obtained positions are shown in Table II. Since these three peaks are observed even in 2D packings of highly nonspherical particles one can conclude that structures of local crystallinity can be observed in all of these packings.

Figure 7(b) plots the RDFs of star-shaped particles in 3D packings. The RDF of particles with $\Psi = 0.995$ shows a first

peak at $r/L = 1$ and a second peak at $r/L = 1.9$. These peaks are at the same positions as in the RDF of 2D packings of cross-shaped particles with $\Psi = 0.995$ because both particle shapes are almost spherical and cannot interlock. In 3D packings of star-shaped particles with $\Psi = 0.702$ the first peak is located at $r/L = 0.7$ and the second peak at $r/L = 1.37$. Compared to 2D packings of cross-shaped particles with similar sphericity, the peaks are shifted to lower r/L values. This observation can be explained by the fact that star-shaped particles in 3D packings have additional degrees of freedom compared to cross-shaped particles in 2D packings allowing closer packing configurations in 3D packings. A sketch of the closest packing of star-shaped particles in 3D is shown in Fig. 7(b). The closest distance (J_1) between the centers of two star-shaped particles in the packing configuration shown in Fig. 7(b) is

$$J_1 = \sqrt{3}d_p. \quad (12)$$

Hence, in 3D packings of star-shaped particles with $\Psi = 0.702$, the first peak J_1 is expected at $r/L = 0.58$ and the second peak at $r/L = 1.15$. However, the first and second peaks are found at $r/L = 0.7$ and $r/L = 1.37$, respectively. This result indicates that the most likely packing configuration of star-shaped particles in a compressed 3D packing is considerably looser than the closest possible crystalline packing configuration. Hence, 3D packings have a different morphology than 2D packings, as the peak location in the RDF of

TABLE II. Peak positions observed in the RDFs of 2D packings of cross-shaped particles and peak positions calculated according to Eq. (11).

Ψ	First peak	D_1/L	Second peak	D_2/L	Third peak	D_3/L
0.473	0.55	0.55	1.12	1.11	1.66	1.66
0.518	0.58	0.57	1.14	1.14	1.73	1.71
0.585	0.62	0.61	1.25	1.21	1.82	1.82
0.754	0.76	0.75	1.50	1.49	2.23	2.24
0.995	1.00	0.98	1.91	1.95	None	2.93

2D packings of cross-shaped particles agrees very well with the closest possible crystalline packing configuration which, however, is not the case for 3D packings.

Additionally, when comparing the RDF of 2D and 3D packings, one finds that the height of the peaks in the RDF of 3D packings is lower than in 2D packings, a further sign of a reduced crystallinity when introducing an additional dimension. The reduced peak height is particularly noticeable when comparing the RDF of cross-shaped particles with $\Psi = 0.754$ [2D packing, Fig. 7(a)] with the RDF of star-shaped particles with $\Psi = 0.702$ [3D packings, Fig. 7(b)]. Even a third peak is visible in the RDF of the 2D packing ($\Psi = 0.754$), whereas a third peak is absent in the RDF of a 3D packing ($\Psi = 0.754$). The reduction in crystallinity in 3D packings is more pronounced for particles of lower sphericity, i.e., $\Psi < 0.702$ ($\Psi < \Psi_{\text{crit}}$); in such packings even the first peak in the RDF disappears completely, indicating an amorphous packing structure. A reduced peak height in the RDF of packings of rodlike particles with decreasing particle sphericity has also been observed in previous works [53–55].

To summarize, the crystallinity of 3D packings of star-shaped particles decreases with decreasing particle sphericity. In 2D packings of cross-shaped particles, however, such a decrease in crystallinity with decreasing sphericity could not be observed. The data in Fig. 7 show that interlocked, crystalline configurations are found in 2D packings of cross-shaped particles with $\Psi < 0.7$, whereas such configurations do not seem to be present to a large extent in 3D packings of star-shaped particles with $\Psi < 0.7$. This can be explained by considering that 3D star-shaped particles have three additional degrees of freedom (one translational degree and two rotational), compared to 2D cross-shaped particles. It is therefore less likely that star-shaped particles, when dropped into a 3D container followed by compression will configure themselves into a highly crystalline packing.

D. Linking force distributions to packing morphology

We described above that in 3D packings, below a critical value of $\Psi < \Psi_{\text{crit}} = 0.7$, the length of the exponential tail of the contact force distribution increases with decreasing particle sphericity. The increasing length of the exponential tail in 3D packings (and not in 2D packings) for sphericities $\Psi < 0.702$ seems to coincide with the disappearance of peaks in the RDF. To understand this observation, we revisit the work by Luding [17], who used the DEM to investigate particle stresses of monodisperse and polydisperse packings of disks in a perfectly hexagonal 2D lattice. For perfectly monodisperse particles, a uniform particle stress distribution was observed. However, as soon as some polydispersity was introduced, by varying the disk diameter by a small amount ($\pm 0.33\%$), localized force chains were observed in the particle packing. Luding [17] also observed that the probability of large particle stresses to occur increases with increasing polydispersity; i.e., the length of the exponential tail of the particle stress distribution increases with increasing polydispersity. One can interpret the findings of the present work as complementary to Luding's [17] results for nonspherical particles; i.e., a decreasing crystallinity of the packing (induced by either polydispersity or nonsphericity) leads to wider, less

homogeneous, contact force and particle stress distributions, provided that the following two assumptions hold: (1) The introduction of polydispersity does lead to a reduction in crystallinity and (2) the behavior of the particle stress distribution, $P(i)$, depending on particle sphericity is very similar to that of the contact force distributions, $P(f)$.

Concerning the first assumption, there is indeed evidence of reduced peak heights in the RDF of a hexagonal packing with 5% polydispersity, when compared to the RDF of a monodisperse packing [56]. The reduced peak height hints toward a reduced crystallinity in polydisperse packings; however, further research is required to confirm the assumption.

To confirm the second assumption, that the exponential decay of the particle stress distribution is similar to the decay of the contact force distribution, one can compare $P(f)$ and $P(i)$, i.e., the probability distribution of the normalized first stress invariant $i = I_{1,i}/\langle I_1 \rangle$ shown in Fig. 8. Generally, the shape of $P(i)$ is similar to the shape of $P(f)$, i.e., for 2D packings distributions of type A and for 3D packings of low-sphericity particles distributions of type B are obtained. For high-sphericity ($\Psi > 0.7$) cross-shaped particles in 2D packings [Fig. 8(a)], the distributions exhibit a pronounced peak at $i = 1$, which disappears for $\Psi < \Psi_{\text{crit}} = 0.7$ as $\lim_{i \rightarrow 0} P(i)$ increases with decreasing Ψ . Specifically, in 3D packings of star-shaped particles, $P(i)$ has a type A-like distribution for $\Psi > 0.7$ (peak at $i = 1$ and an exponential tail of similar length as in 2D packings), and no particle experiences a stress invariant with a magnitude of more than 6 times the mean. However, for 3D packings of star-shaped particles with $\Psi < \Psi_{\text{crit}}$, the shape of $P(i)$ changes to a type B distribution and the length of the exponential tail of $P(i)$ increases with decreasing particle sphericity. The steep increase of $\lim_{i \rightarrow 0} P(i)$ implies that there is an increasing number of particles that experience only a very small fraction of the load that is put on the packing by uniaxial compression. At the same time, owing to the increasing length of the exponential tail, some particles experience stresses that are significantly higher than the mean. These trends match the behavior of $P(f)$, as described further above.

The transition of $P(i)$ to a type B distribution in 3D packings of star-shaped particles for decreasing sphericity is attributed to an increasing frequency of contacts between the flat parts of the arms protruding from the particles [Fig. 6(c)]. Such contacts are only possible for star-shaped particles with $\Psi < \Psi_{\text{crit}}$, whereas for $\Psi \geq \Psi_{\text{crit}}$ all contacts between star-shaped particles involve the hemispherical end caps of the spherocylinders. Particles forming contacts between the flat parts of the spherocylinders are less likely to rearrange during uniaxial compression. This effect can also be interpreted as an increased apparent friction coefficient between particles. Such particles are more likely to jam during uniaxial compression, instead of rearranging into a configuration which would reduce the stress acting on the particle. As a consequence, high stresses can build up which results in an increased length of the tail of $P(i)$. The buildup of stresses in some particles leaves other particles to contribute little to the stress transmission in the packing leading in turn to an increase of $\lim_{i \rightarrow 0} P(i)$ with increasing apparent friction [57].

To summarize, the dependence of the length of the exponential tail of $P(i)$ on particle sphericity is very similar to the respective behavior of $P(f)$. Hence, our results can indeed be

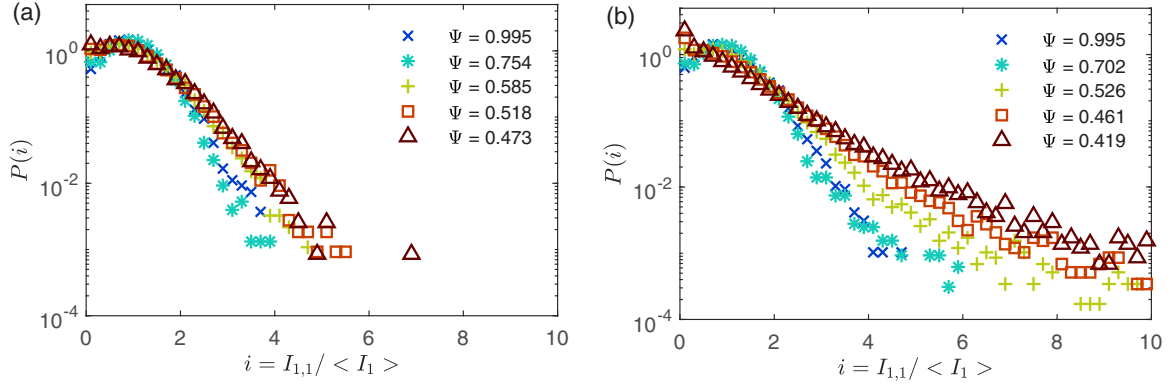


FIG. 8. Probability distributions of the normalized first stress invariants $P(i)$ as a function of particle sphericity in (a) 2D and (b) 3D packings. The normalized first stress invariants i are obtained by normalizing the first stress invariants $I_{1,i}$ by $\langle I_1 \rangle$.

considered as complementary to Luding's [17] observation on the effect of polydispersity on the stress distribution in particle packings; i.e., a decreasing crystallinity (due to increasing nonsphericity or polydispersity) leads to an extended tail of the contact force and particle stress distributions.

IV. CONCLUSIONS

This work investigated compressed 2D and 3D packings of nonspherical, nonconvex, cross- and star-shaped particles using a recently developed DEM. Such nonconvex particles can interlock forming packings that may sustain compressive and tensile forces despite containing purely non-cohesive particles. The particle sphericity (Ψ) was varied in the range $\Psi = 0.42$ – 1 . The morphology of the packings was investigated by calculating the radial distribution function (RDF). Through the RDF we have established a link between the packing morphologies and the contact force probability distributions as expressed by the decay exponent k .

In 2D packings of cross-shaped particles a linear decrease of k was observed, from $k = 1.42$ for $\Psi = 0.995$ to $k = 1.32$ for $\Psi = 0.47$. For pseudo-2D and -3D packings of star-shaped particles k is independent of the sphericity ($k = 1.38 \pm 0.14$) for $\Psi > 0.7$; however, for smaller sphericities (i.e., $\Psi < 0.7$) the magnitude of k decreases exponentially with decreasing Ψ . These findings establish a connection between the results of previous works [13,14,26] on compressed packings of nonspherical particles. This allows us to establish the following general correlations between Ψ and the heterogeneity of the distribution of the contact forces expressed by the magnitude of k :

(1) In compressed 3D packings, the distribution of contact forces in the normal direction becomes increasingly heterogeneous; i.e., the length of the exponential tail increases

exponentially with decreasing particle sphericity, independent of the specific particle shape.

(2) In 2D packings the influence of particle sphericity on the distribution of the contact force distribution in the normal direction is small. In contrast to the exponentially decreasing k with decreasing Ψ in 3D packings, the decrease of k with decreasing Ψ in 2D packings is linear.

The heterogeneity of the contact force distribution needs to be considered when designing particles for specific applications such as aleatory construction for which nonconvex particles with low sphericity (e.g., $\Psi = 0.45$ [13]) are desired. Such particles need to be able to withstand the highest contact forces, which can reach values that are an order of magnitude higher than the mean contact force.

We further establish a link between the increasing heterogeneity of the distribution of the contact forces and the packing morphology in packings of nonspherical particles. We have demonstrated that the increasing heterogeneity in the contact force distributions with decreasing sphericity correlates with a decreasing crystallinity of the packings. The link between a decreasing packing crystallinity and more heterogeneous contact force distributions has been postulated previously by Luding [17] for spherical particles, when assessing the effect of polydispersity on the homogeneity of the particle stress distributions. Hence, our results can be interpreted as complementary to this previous observation providing further evidence that a reduced packing crystallinity, through either an increase of domain dimensionality, particle nonsphericity, or polydispersity, leads to a more heterogeneous stress distribution.

ACKNOWLEDGMENT

This work has been financed by the Swiss National Science Foundation Grants No. 200021_157122/1 and No. 200020_182692.

- [1] B. Indraratna, D. Ionescu, and H. D. Christie, *J. Geotech. Geoenviron. Eng.* **124**, 439 (1998).
- [2] L. D. Poulikakos and M. N. Partl, *J. Microsc.* **240**, 145 (2010).

- [3] N. Kaliyan, R. V. Morey, and D. R. Schmidt, *Biomass Bioenergy* **55**, 322 (2013).
- [4] R. Linemann, J. Runge, M. Sommerfeld, and U. Weißgüttel, *Part. Part. Syst. Charact.* **21**, 261 (2004).

- [5] C.-h. Liu, S. R. Nagel, D. A. Schecter, S. N. Coppersmith, S. Majumdar, O. Narayan, and T. A. Witten, *Science* **269**, 513 (1995).
- [6] T. S. Majumdar and R. P. Behringer, *Nature* **435**, 1079 (2005).
- [7] A. Drescher and G. de Josselin de Jong, *J. Mech. Phys. Solids* **20**, 337 (1972).
- [8] R. C. Hidalgo, C. U. Grosse, F. Kun, H. W. Reinhardt, and H. J. Herrmann, *Phys. Rev. Lett.* **89**, 205501 (2002).
- [9] A. Rechenmacher, S. Abedi, and O. Chupin, *Geotech. London* **60**, 343 (2010).
- [10] M. Oda and H. Kazama, *Geotechnique* **48**, 465 (1998).
- [11] H. Laubie, F. Radjai, R. Pellenq, and F.-J. Ulm, *Phys. Rev. Lett.* **119**, 075501 (2017).
- [12] D. M. Mueth, H. M. Jaeger, and S. R. Nagel, *Phys. Rev. E* **57**, 3164 (1998).
- [13] K. A. Murphy, N. Reiser, D. Choksy, C. E. Singer, and H. M. Jaeger, *Granular Matter* **18**, 26 (2016).
- [14] B. Saint-Cyr, J.-Y. Delenne, C. Voivret, F. Radjai, and P. Sornay, *Phys. Rev. E* **84**, 041302 (2011).
- [15] E. Azéma and F. Radjaï, *Phys. Rev. E* **85**, 031303 (2012).
- [16] A. Abed Zadeh, J. Barés, T. A. Brzinski, K. E. Daniels, J. Dijkstra, N. Docquier, H. O. Everitt, J. E. Kollmer, O. Lantsoght, D. Wang, M. Workamp, Y. Zhao, and H. Zheng, *Granular Matter* **21**, 1 (2019).
- [17] S. Luding, *Phys. Rev. E* **55**, 4720 (1997).
- [18] J. Jose, A. van Blaaderen, A. Imhof, and A. Imhof, *Phys. Rev. E* **93**, 062901 (2016).
- [19] E. Olsson, D. Jelagin, and M. N. Partl, *Road Mater. Pavement Des.* **20**, S604 (2019).
- [20] P. A. Cundall and O. D. L. Strack, *Geotechnique* **29**, 47 (1979).
- [21] Y. Zhao, K. Liu, M. Zheng, J. Barés, K. Dierichs, A. Menges, and R. P. Behringer, *Granular Matter* **18**, 24 (2016).
- [22] Y. Zhao, J. Barés, and J. E. S. Socolar, *Phys. Rev. E* **101**, 062903 (2020).
- [23] K. Dierichs and A. Menges, *Granular Matter* **18**, 25 (2016).
- [24] K. Murphy, L. Roth, D. Peterman, and H. Jaeger, *Archit. Des.* **87**, 74 (2017).
- [25] P. Aejmelaeus-Lindström, J. Willmann, S. Tibbits, F. Gramazio, and M. Kohler, *Granular Matter* **18**, 28 (2016).
- [26] J. Q. Gan, Z. Y. Zhou, and A. B. Yu, *Powder Technol.* **320**, 610 (2017).
- [27] G. Lu, J. R. Third, and C. R. Müller, *Chem. Eng. Sci.* **127**, 425 (2015).
- [28] H. P. Zhu, Z. Y. Zhou, R. Y. Yang, and A. B. Yu, *Chem. Eng. Sci.* **62**, 3378 (2007).
- [29] Y. Guo, C. Wassgren, W. Ketterhagen, B. Hancock, and J. Curtis, *Powder Technol.* **228**, 193 (2012).
- [30] G. Lu, J. R. Third, and C. R. Müller, *Granular Matter* **16**, 107 (2014).
- [31] G. Lu, R. C. Hidalgo, J. R. Third, and C. R. Müller, *Granular Matter* **18**, 34 (2016).
- [32] G. Lu and C. R. Müller, *Granular Matter* **22**, 50 (2020).
- [33] V. J. Lumelsky, *Inf. Process. Lett.* **21**, 55 (1985).
- [34] T. Schwager and T. Pöschel, *Granular Matter* **9**, 465 (2007).
- [35] R. Kumar, A. Sarkar, W. Ketterhagen, B. Hancock, J. Curtis, and C. Wassgren, *AIChE J.* **64**, 1986 (2018).
- [36] M. Kodam, R. Bharadwaj, J. Curtis, B. Hancock, and C. Wassgren, *Chem. Eng. Sci.* **64**, 3466 (2009).
- [37] D. Höhner, S. Wirtz, H. Kruggel-Emden, and V. Scherer, *Powder Technol.* **208**, 643 (2011).
- [38] T. Kidokoro, R. Arai, and M. Saeki, *Granular Matter* **17**, 743 (2015).
- [39] S. Luding, in *Physics of Dry Granular Media*, edited by H. J. Herrmann (Springer Netherlands, Dordrecht, 1998), pp. 285–304.
- [40] L. E. Silbert, D. Ertas, G. S. Grest, T. C. Halsey, D. Levine, and S. J. Plimpton, *Phys. Rev. E* **64**, 14 (2001).
- [41] J. Third, Ph.D. thesis, University of Cambridge, 2009.
- [42] J. R. Third and C. R. Müller, *Phys. Rev. E* **86**, 061314 (2012).
- [43] See Supplemental Material at <http://link.aps.org/supplemental/10.1103/PhysRevE.102.062902> for details on the packing density, the conversion between particle sphericity and aspect ratio, the influence of particle friction and wall friction on the packing, and enhanced visualizations of the closest possible particle configurations.
- [44] M. J. Jiang, J. M. Konrad, and S. Leroueil, *Comput. Geotech.* **30**, 579 (2003).
- [45] L. Meng, C. Wang, and X. Yao, *Phys. A (Amsterdam, Neth.)* **490**, 212 (2018).
- [46] I. Malinouskaya, V. V. Mourzenko, J.-F. Thovert, and P. M. Adler, *Phys. Rev. E* **80**, 011304 (2009).
- [47] Y. Yang, J. F. Wang, and Y. M. Cheng, *Particuology* **25**, 23 (2016).
- [48] A. Wachs, L. Girolami, G. Vinay, and G. Ferrer, *Powder Technol.* **224**, 374 (2012).
- [49] F. Ludewig and N. Vandewalle, *Phys. Rev. E* **85**, 051307 (2012).
- [50] H. Pourtavakoli, E. J. R. Parteli, and T. Pöschel, *New J. Phys.* **18**, 73049 (2016).
- [51] S. Zhao, N. Zhang, X. Zhou, and L. Zhang, *Powder Technol.* **310**, 175 (2017).
- [52] R. J. Bathurst and L. Rothenburg, *J. Appl. Mech.* **55**, 17 (1988).
- [53] S. R. Williams and A. P. Philipse, *Phys. Rev. E* **67**, 051301 (2003).
- [54] R. C. Hidalgo, I. Zuriguel, D. Maza, and I. Pagonabarraga, *J. Stat. Mech.* (2010) P06025.
- [55] C. Ferreira-Córdova and J. S. Van Duijneveldt, *J. Chem. Eng. Data* **59**, 3055 (2014).
- [56] S. E. Phan, W. B. Russel, J. Zhu, and P. M. Chaikin, *J. Chem. Phys.* **108**, 9789 (1998).
- [57] N. Estrada, A. Taboada, and F. Radjaï, *Phys. Rev. E* **78**, 021301 (2008).